



# Photocatalytic degradation of bisphenol A by oxygen-rich and highly visible-light responsive $\text{Bi}_{12}\text{O}_{17}\text{Cl}_2$ nanobelts

Chu-Ya Wang, Xing Zhang\*, Hai-Bin Qiu, Wei-Kang Wang, Gui-Xiang Huang, Jun Jiang, Han-Qing Yu\*

CAS Key Laboratory of Urban Pollutant Conversion, Department of Chemistry, University of Science & Technology of China, Hefei 230026, China



## ARTICLE INFO

### Article history:

Received 13 June 2016

Received in revised form 18 July 2016

Accepted 30 July 2016

Available online 1 August 2016

### Keywords:

Bisphenol A

$\text{Bi}_{12}\text{O}_{17}\text{Cl}_2$  nanobelt

Oxygen rich

Photoacatalytic

Visible light

## ABSTRACT

Visible light responsive photocatalysts can directly harvest energy from solar light, offering a desirable way to resolve environmental pollution problems through utilizing solar energy. Bismuth oxychloride ( $\text{BiOCl}$ ) with a band gap of about 3.4 eV is widely recognized as an effective photocatalyst for the degradation of organic dye molecules under visible light irradiation, but such a photocatalytic degradation has to be assisted by dye-sensitization. Thus, preparation of  $\text{BiOCl}$  photocatalyst to achieve visible light response without dye-sensitization is greatly desired, as this would greatly expand their practical applications for the degradation of non-dye pollutants. In this work, oxygen-rich  $\text{Bi}_{12}\text{O}_{17}\text{Cl}_2$  nanobelts with a band gap of 2.07 eV were synthesized by using a solvothermal route, and their photocatalytic performance was evaluated through photodegrading a colorless contaminant bisphenol A (BPA) in an aqueous solution. In comparison with  $\text{BiOCl}$ , which is not sensitive to visible light, the oxygen-rich  $\text{Bi}_{12}\text{O}_{17}\text{Cl}_2$  nanobelts exhibited a drastically enhanced visible-light photoreactivity and were also superior to the well-known photocatalyst  $\text{TiO}_2$  (P25). The greatly enhanced photocatalytic performance of the  $\text{Bi}_{12}\text{O}_{17}\text{Cl}_2$  nanobelts was attributed to their efficient visible light absorption. Our findings might be helpful to explore visible light bismuth-based photocatalysts for pollutant degradation and water treatment.

© 2016 Elsevier B.V. All rights reserved.

## 1. Introduction

Photocatalytic process, as a green technology, has attracted extensive interests in the fields of water splitting and pollutant degradation [1–4].  $\text{TiO}_2$  has been recognized as the most efficient photocatalyst for the degradation of organic pollutants in water and wastewater [5–7]. However, the band gap of  $\text{TiO}_2$  larger than 3.0 eV limits its photoactivity to the UV region, making  $\text{TiO}_2$  an inefficient photocatalyst for solar light utilization [8,9]. Thus, efforts should be made to overcome such a limitation, optimize the use of solar energy, and explore new photocatalysts.

Bismuth oxychloride, as a potential photocatalyst, has drawn growing attention because of its low costs and high efficiency [10–16]. For example,  $\text{BiOCl}$  single-crystalline nanosheets with exposing (001) facets exhibited a higher activity than those exposing (010) facets for direct photoexcitation-induced pollutant degradation under UV light [12]. The ultrathin  $\text{BiOCl}$  nanosheets

exhibited an excellent direct photoexcitation-induced photocatalytic activity under UV light irradiation [17]. However, the synthesis of one-dimensional structure bismuth oxychloride with reduced band gap for harvesting visible light remains a great challenge.

It is well known that the valence band (VB) in bismuth oxychloride is mainly composed of Bi 6p, O 2p and Cl 3p orbitals, while the conduction band (CB) is based on Bi 6s and Cl 3s orbitals [18,19]. Theoretically, tuning the ratio of halides should modulate the band structures. Recently, we have successful synthesized series  $\text{BiOCl}_x\text{Br}_{1-x}$  solid solution [20], and  $\text{BiOBr}_x\text{I}_{1-x}$  solid solution nanoplates with tunable band structures [21]. Inspired by these previous works, we assume that bismuth oxychloride with a value of Cl:O ratio might reduce its CB or VB position and then exhibit a decrease in the band gap energy ( $E_g$ ), resulting in stronger response to visible light irradiation than  $\text{BiOCl}$ . Up to now, synthesis of two-dimensional oxygen-rich bismuth oxychloride nanosheets, including  $\text{Bi}_{12}\text{O}_{15}\text{Cl}_6$  nanoplates [19,22,23],  $\text{Bi}_3\text{O}_4\text{Cl}$  nanoplates [11,24],  $\text{Bi}_{12}\text{O}_{17}\text{Cl}_2$  nanosheets [25] and  $\text{Bi}_{24}\text{O}_{31}\text{Cl}_{10}$  nanoplates [26,27], has been reported, but information about the synthesis of one-dimensional (1D) oxygen-rich bismuth oxychloride nanobelts is still limited [28]. In a previous work,  $\text{Bi}_{24}\text{O}_{31}\text{Cl}_{10}$  nanobelts were

\* Corresponding authors.

E-mail addresses: [zhangx@ustc.edu.cn](mailto:zhangx@ustc.edu.cn) (X. Zhang), [\(H.-Q. Yu\).](mailto:hqyu@ustc.edu.cn)

synthesized by using cetanetyl trimethyl ammonium chloride as Cl source and surfactant [28], but surfactants usually have a negative impact on the photocatalytic activity. Furthermore,  $\text{Bi}_{12}\text{O}_{17}\text{Cl}_2$  consisted of some belts was synthesized using a hydrothermal method [29]. In their work, water was used as the solvent and the morphology of the resulting products was not homogeneous.  $\text{Bi}_{12}\text{O}_{17}\text{Cl}_2$  nanowires were also prepared via a two-step process by thermally treating  $\alpha\text{-Bi}_2\text{O}_3$  nanowires precursor with HCl [30]. However, a simple, highly-efficient and facile method of synthesizing oxygen-rich bismuth oxychloride with a belt-like structure without using any surfactants is highly desired.

In this work,  $\text{Bi}_{12}\text{O}_{17}\text{Cl}_2$  nanobelts with a narrowed band gap were synthesized via a facile solvothermal route. The prepared  $\text{Bi}_{12}\text{O}_{17}\text{Cl}_2$  nanobelts photocatalyst was characterized and their photocatalytic performance was evaluated by photocatalyzing the degradation of a colorless contaminant bisphenol A (BPA) in an aqueous solution in comparison with  $\text{BiOCl}$  and a well-known photocatalyst  $\text{TiO}_2$  (P25). The photocatalytic mechanism was explored and the degradation model of BPA over  $\text{Bi}_{12}\text{O}_{17}\text{Cl}_2$  nanobelts was established on the basis of the identified active species and the degradation pathway. In this way, an efficient photocatalyst was developed for pollutant degradation and water treatment.

## 2. Materials and methods

### 2.1. Synthesis of $\text{Bi}_{12}\text{O}_{17}\text{Cl}_2$ nanobelts

All chemicals used in this work were of analytical grade and purchased from Shanghai Chemical Reagent Co., China. In a typical procedure, 0.485 g  $\text{Bi}(\text{NO}_3)_3 \cdot 5\text{H}_2\text{O}$  (1 mmol) was added into 5 mL ethylene glycol. Under 10-min vigorous stirring and sonication, the mixture was dispersed to form a homogeneous solution. Meanwhile, 0.162 g  $\text{NH}_4\text{Cl}$  (3 mmol) and 0.400 g NaOH (10 mmol) were added into 30 mL distilled water under vigorous stirring for 5 min to form a homogeneous solution in parallel. Then, the above two solutions were mixed with stirring, and a white suspension was formed immediately. The white suspension was transferred into a 50 mL autoclave with Teflon linear, which was heated at 140 °C for 12 h, and then naturally cooled to ambient temperature. The resulting yellow solid powder was collected through centrifugation and washed with distilled water and absolute alcohol for three times to remove residual ions and organics. The product was then dried at 80 °C for 6 h prior to characterization. For comparison,  $\text{BiOCl}$  was also prepared using 0.485 g  $\text{Bi}(\text{NO}_3)_3 \cdot 5\text{H}_2\text{O}$  (1 mmol) and 0.054 g  $\text{NH}_4\text{Cl}$  (1 mmol) by the same procedure without adding NaOH.

### 2.2. Physicochemical characterization of $\text{Bi}_{12}\text{O}_{17}\text{Cl}_2$ nanobelts

The X-ray powder diffraction (XRD) patterns of the samples were obtained on a Philips X'Pert PRO SUPER diffractometer equipped with graphite monochromatized  $\text{Cu K}\alpha$  radiation ( $\lambda = 1.541874 \text{ \AA}$ ). The scanning electron microscopy (SEM) images of the samples were taken with an X-650 scanning electron micro analyzer and a JSM-6700F field emission SEM (JEOL Co., Japan). The transmission electron microscopy (TEM) images of the samples were recorded on a TEM (JEM-2011, JEOL Co., Japan), using an electron kinetic energy of 200 kV. The high-resolution transmission electron microscopy (HRTEM) images and selected area electron diffraction (SAED) patterns were taken on an HRTEM (2010, JEOL Co., Japan) at an acceleration voltage of 200 kV. The chemical compositions and the valence states of constituent elements were analyzed by X-ray photoelectron spectroscopy (XPS) (ESCALAB250, Thermo Fisher Inc., USA). The UV-vis diffuse reflection spectra (UV-vis DRS) were measured using a UV/Vis spectrophotometer (Solid 3700, Shimadzu Co., Japan). The electron spin resonance (ESR)

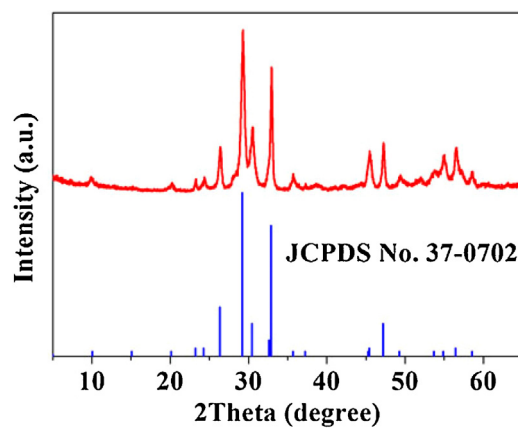


**Fig. 1.** XRD patterns of  $\text{Bi}_{12}\text{O}_{17}\text{Cl}_2$  sample.

(JES-FA200, JEOL Co., Japan) was used to detect free radicals. The surface area was measured by using the Brunauer–Emmett–Teller (BET) method with a Builder 4200 instrument (Tristar II 3020M, Micromeritics Co., USA).

### 2.3. Photocatalytic degradation of BPA by $\text{Bi}_{12}\text{O}_{17}\text{Cl}_2$ nanobelts

The photocatalytic activity of the  $\text{Bi}_{12}\text{O}_{17}\text{Cl}_2$  nanobelts for the degradation of BPA was evaluated using a 500 W Xe arc lamp with a 420 nm cutoff filter as the light source at ambient temperature, and the radiation flux was  $94 \text{ mW cm}^{-2}$ . Before the tests, 20 mg of  $\text{Bi}_{12}\text{O}_{17}\text{Cl}_2$  nanobelts as a photocatalyst was added into 40 mL aqueous solution containing  $10 \text{ mg L}^{-1}$  BPA, and stirred in dark for 60 min to ensure sufficient adsorption/desorption equilibrium. Then, samples were collected at given time intervals under light irradiation and continuously magnetic stirring. BPA concentration was measured using a HPLC (1260 Infinity, Agilent Inc., USA) with an Agilent Eclipse XDB-C18 column ( $4.6 \times 150 \text{ mm}$ ) and the column temperature of 30 °C. To measure the concentrations of BPA, 50% acetonitrile and 50% deionized water (containing 0.1% formic acid) were used as the mobile phase at a flow rate of  $1.0 \text{ mL min}^{-1}$ , and the detection wavelength was 273 nm. A liquid chromatography-mass spectrometry (LC-MS) (6460 LC/QQQ, Agilent Inc., USA) was used to determine the intermediate products from BPA degradation. All the detecting conditions of LC-MS were the same as that of HPLC except the mobile phase, which was 50% acetonitrile and 50% deionized water (without formic acid). The total organic carbon (TOC) concentration was measured using a TOC analyzer (Multi N/C 2100, Analytik Jena AG, Germany).

## 3. Results and discussion

### 3.1. Characteristics of $\text{Bi}_{12}\text{O}_{17}\text{Cl}_2$ nanobelts

XRD analysis was used to characterize the phase of the sample. Fig. 1 shows the XRD pattern of the sample, where all the diffraction peaks could be indexed to  $\text{Bi}_{12}\text{O}_{17}\text{Cl}_2$  (JCPDS card No. 37-0702). No peaks of any other phases were detected, indicating the purity of the final product. The strong and sharp reflection peaks suggest that the as-prepared sample was well crystallized.

The morphology of the  $\text{Bi}_{12}\text{O}_{17}\text{Cl}_2$  sample was imaged using SEM and TEM. The SEM images (Fig. 2a and b) reveal that the sample possessed a large scale of belt-like structure with a length of several micrometers and a thickness of approximately 20 nm. The TEM images (Fig. 2c) further confirm the belt-like structure of the  $\text{Bi}_{12}\text{O}_{17}\text{Cl}_2$  sample. Almost each nanobelt had a uniform width along its entire length and the typical widths of the nanobelts were in a range of 80–500 nm. Fig. 2d shows a typical single bending

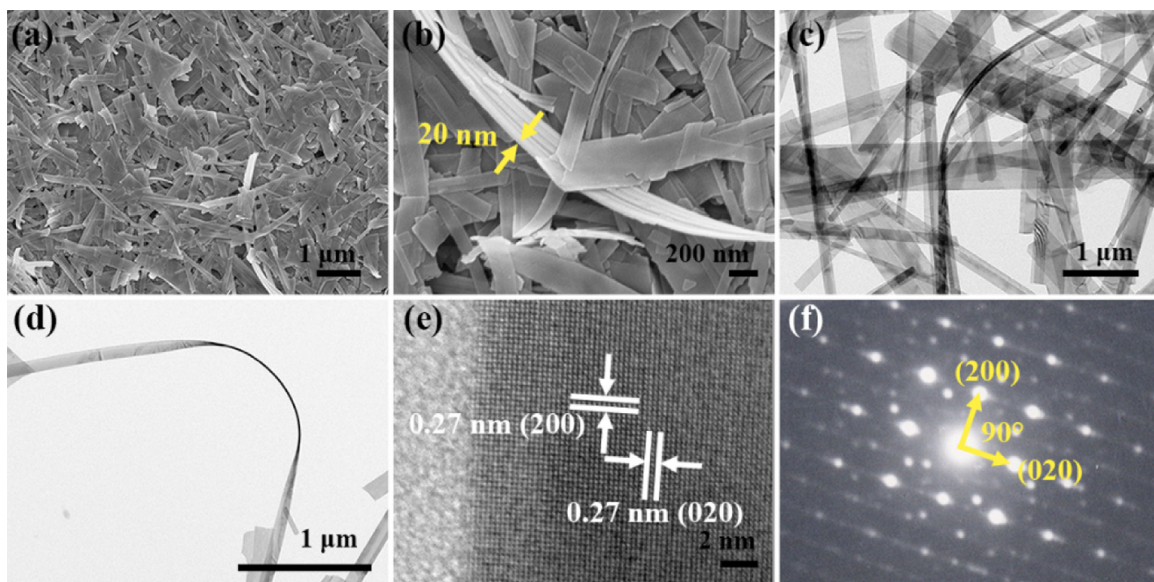


**Fig. 2.** (a) Low magnification and (b) high magnification SEM images, (c) low magnification and (d) high magnification TEM images, (e) HRTEM image and (f) the corresponding SAED of the  $\text{Bi}_{12}\text{O}_{17}\text{Cl}_2$  nanobelts.

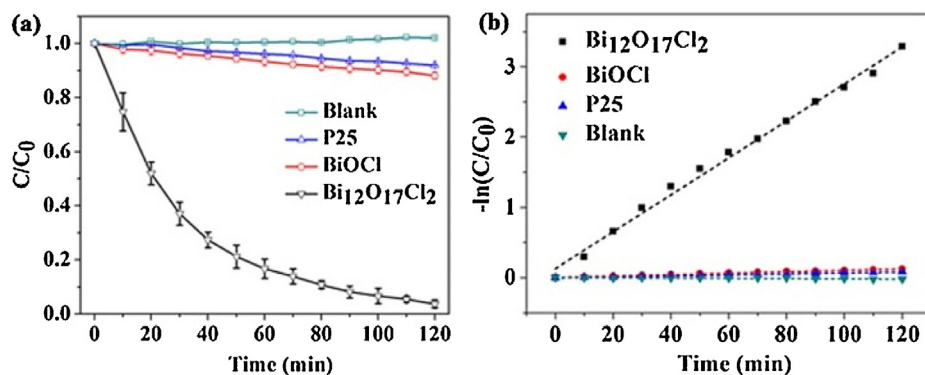


**Fig. 3.** (a) Photocatalytic degradation curves, and (b) kinetic curves of  $\text{Bi}_{12}\text{O}_{17}\text{Cl}_2$  nanobelts,  $\text{BiOCl}$ ,  $\text{TiO}_2$  (P25), and blank test under visible light irradiation, respectively.

nanobelt with a length and width of 5  $\mu\text{m}$  and 90 nm, respectively. The crystal structure of  $\text{Bi}_{12}\text{O}_{17}\text{Cl}_2$  was further characterized using HRTEM. The HRTEM image (Fig. 2e), which was taken from the edge of a single nanobelt, reveals a high crystallinity and clear lattice fringes. The continuous lattice fringes with an interplanar lattice spacing of 0.27 nm, matched well with the (200) and (020) atomic planes of  $\text{Bi}_{12}\text{O}_{17}\text{Cl}_2$ . As depicted in Fig. 2f, the SAED pattern displays a spot pattern, indicating the single-crystalline characteristic of the obtained nanobelts. The angle of adjacent spots labelled in the SAED pattern was 90°, which is identical to the theoretical value of the angle between the (200) and (020) atomic planes of  $\text{Bi}_{12}\text{O}_{17}\text{Cl}_2$ .

In a previous work,  $\text{Bi}_{12}\text{O}_{17}\text{Cl}_2$  belts were synthesized using a hydrothermal method with water as the solvent [29], and some sheet-like products were obtained. In another previous work,  $\text{Bi}_{12}\text{O}_{17}\text{Cl}_2$  nanosheets were synthesized using  $\text{BiCl}_3$  as the raw material [25], and the morphology of the resulting product was 2D nanosheets, rather than 1D nanobelts. In our work, ethylene glycol, instead of water, was used to control the morphology of the product. In the presence of ethylene glycol,  $\text{Bi}(\text{NO}_3)_3$  could be dispersed easily and evenly with vigorous sonication treatment, contributing to the homogeneousness of the  $\text{Bi}_{12}\text{O}_{17}\text{Cl}_2$  belts.

### 3.2. Photocatalytical degradation of BPA over $\text{Bi}_{12}\text{O}_{17}\text{Cl}_2$ nanobelts

The photocatalytic activities of  $\text{Bi}_{12}\text{O}_{17}\text{Cl}_2$  nanobelts,  $\text{BiOCl}$  and  $\text{TiO}_2$  (P25) were compared by examining their photocatalytic degradation of BPA under visible light irradiation ( $\lambda > 420 \text{ nm}$ ) over time (Fig. 3a). BPA was selected as the target compound because it is a widely present environmental contaminant with endocrine-disrupting effects [31–34]. Obviously, BPA could not be readily degraded without any photocatalysts, indicating that BPA itself was stable under visible light irradiation.  $\text{Bi}_{12}\text{O}_{17}\text{Cl}_2$  nanobelts were able to degrade more than 95% BPA after 120-min visible light irradiation. In comparison,  $\text{BiOCl}$  and  $\text{TiO}_2$  (P25) degraded only less than 10% of BPA within 120 min. The reaction kinetics of all samples could be fitted well by the pseudo first order rate model with a good correlation coefficient (Fig. 3b). The calculated  $k$  values for  $\text{Bi}_{12}\text{O}_{17}\text{Cl}_2$ ,  $\text{BiOCl}$  and  $\text{TiO}_2$  (P25) were 0.0263, 0.0010, and 0.0007  $\text{min}^{-1}$ , respectively.

To evaluate the effect of surface area on the photocatalytic activities of the catalysts [35,36], the nitrogen adsorption/desorption isotherms of  $\text{Bi}_{12}\text{O}_{17}\text{Cl}_2$ ,  $\text{BiOCl}$  and  $\text{TiO}_2$  (P25) were measured (Fig. S1). The BET surface areas of  $\text{Bi}_{12}\text{O}_{17}\text{Cl}_2$ ,  $\text{BiOCl}$ , and  $\text{TiO}_2$  were

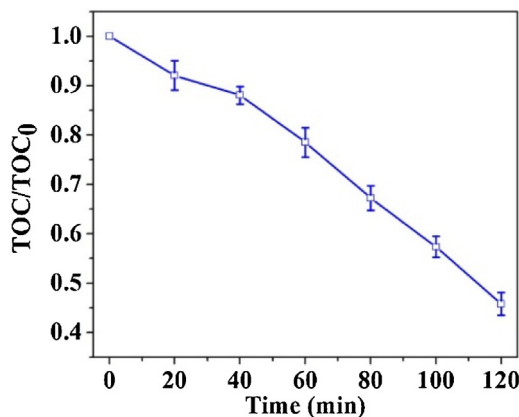


Fig. 4. Reduction of TOC by Bi<sub>12</sub>O<sub>17</sub>Cl<sub>2</sub> nanobelts in the photocatalytic degradation.

6.56, 5.86 and 42.30 m<sup>2</sup> g<sup>-1</sup> respectively. As a result, the surface-area-normalized photocatalytic reaction rate constants of the three photocatalysts were calculated to be 4.0, 0.2, and 0.1 mg m<sup>-2</sup> min<sup>-1</sup>, respectively. The surface-area-normalized reaction rate constant for the Bi<sub>12</sub>O<sub>17</sub>Cl<sub>2</sub> nanobelts was 20 and 40 times higher than that of BiOCl and TiO<sub>2</sub> (P25), respectively. Thus, the photocatalytic activity of Bi<sub>12</sub>O<sub>17</sub>Cl<sub>2</sub> nanobelts was far superior to that of BiOCl and TiO<sub>2</sub> (P25), as the photocatalytic activities of catalysts did not rely on their surface area.

Furthermore, upon 120-min visible light irradiation, the TOC value in the reaction system containing Bi<sub>12</sub>O<sub>17</sub>Cl<sub>2</sub> nanobelts decreased by 50%, indicating that the Bi<sub>12</sub>O<sub>17</sub>Cl<sub>2</sub> nanobelts was effective in mineralizing BPA into CO<sub>2</sub> and H<sub>2</sub>O (Fig. 4). The cycling stability is another important characteristic for catalysts. To investigate the recyclability of Bi<sub>12</sub>O<sub>17</sub>Cl<sub>2</sub> nanobelts, the sample was collected after the photocatalytic reaction and reused five times under the same experimental conditions. The Bi<sub>12</sub>O<sub>17</sub>Cl<sub>2</sub> nanobelts were stable and could maintain its high photocatalytic performance over the five reaction cycles (Fig. S2).

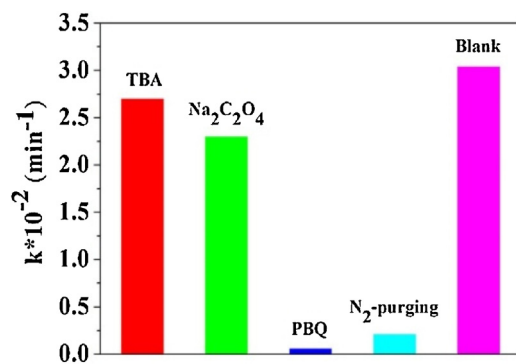


Fig. 5. Kinetic constant of each scavenger.

### 3.3. Active species in the photocatalytical degradation of BPA by Bi<sub>12</sub>O<sub>17</sub>Cl<sub>2</sub> nanobelts

In the present work, the photocatalytic degradation of BPA was likely to occur through the oxidation by •OH, •O<sub>2</sub><sup>-</sup>, or h<sup>+</sup>. To explore the roles of the active species responsible for the BPA removal under visible light irradiation, series experiments by adding various scavengers were conducted. The scavengers used in these tests included sodium oxalate (Na<sub>2</sub>C<sub>2</sub>O<sub>4</sub>) for h<sup>+</sup> [37], tert-butyl alcohol (TBA) for •OH [38], p-benzoquinone (PBQ) for •O<sub>2</sub><sup>-</sup> [23], and N<sub>2</sub>-purging for molecular oxygen [39]. As shown in Fig. 5, the BPA degradation was greatly suppressed by the dose of PBQ and N<sub>2</sub>-purging. The inhibitory efficiencies were estimated to be 1% for TBA, 2% for sodium oxalate, 96% for dissolved oxygen, and 98% for PBQ on the BPA degradation. This result indicates that the contribution of the active species to the photocatalytical degradation of BPA was in the order of •O<sub>2</sub><sup>-</sup> > h<sup>+</sup> > •OH. Thus, it is reasonable to assume that the ability of free radical generation is the vital factor that governs the activity of Bi<sub>12</sub>O<sub>17</sub>Cl<sub>2</sub>, BiOCl and TiO<sub>2</sub> (P25).

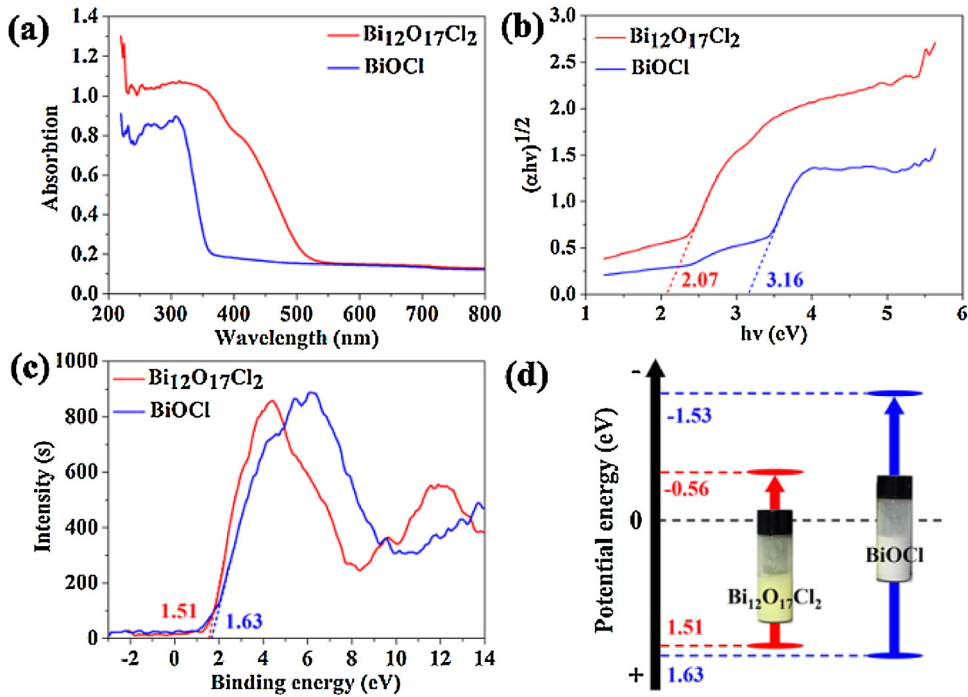
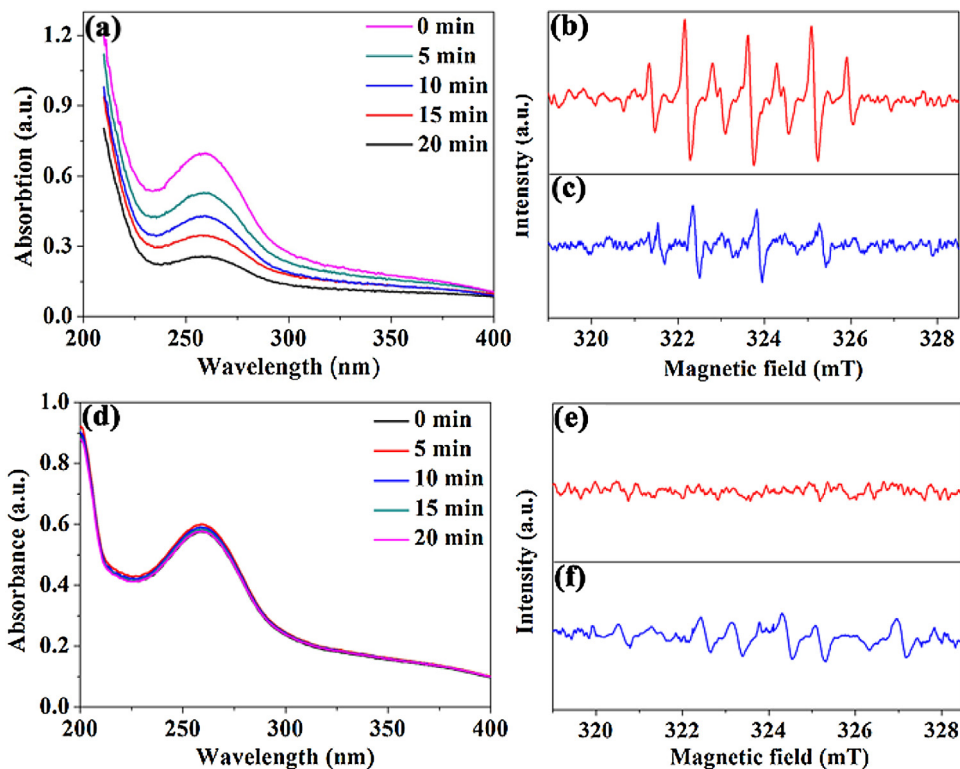
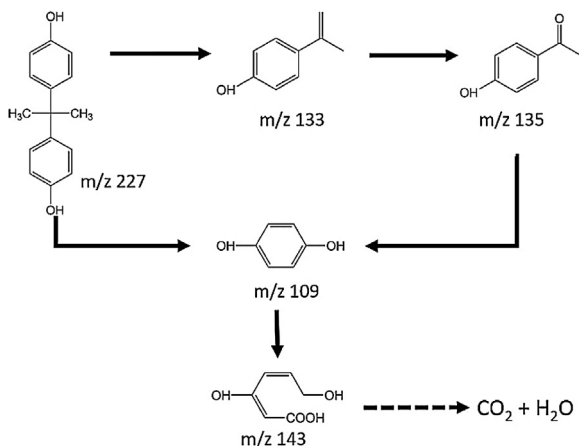


Fig. 6. (a) UV-vis diffuse reflectance spectra, (b) the band gap values, estimated from the plotted curve of  $(\alpha h\nu)^{1/2}$  versus  $h\nu$ , (c) XPS valence band spectrums, and (d) band structures of Bi<sub>12</sub>O<sub>17</sub>Cl<sub>2</sub> and BiOCl and corresponding colours.



**Fig. 7.** (a) UV-vis absorption spectra of NBT of  $\text{Bi}_{12}\text{O}_{17}\text{Cl}_2$ , (b, c) ESR signals of  $\cdot\text{OOH}$  and  $\cdot\text{OH}$  produced by  $\text{Bi}_{12}\text{O}_{17}\text{Cl}_2$ , respectively, (d) UV-vis absorption spectra of NBT of  $\text{BiOCl}$ , (e, f) ESR signals of  $\cdot\text{OOH}$  and  $\cdot\text{OH}$  produced by  $\text{BiOCl}$ , respectively.



**Fig. 8.** Proposed BPA photodegradation pathway by  $\text{Bi}_{12}\text{O}_{17}\text{Cl}_2$  nanobelts.

The active species production is closely related to the electro structure of semiconductor catalysts. The band gap of a semiconductor can be deduced from the equation below [40]:

$$\alpha(h\nu) = A(h\nu - E_g)^n/2 \quad (1)$$

where  $\alpha$ ,  $h\nu$ ,  $E_g$ , and  $A$  are the absorption coefficient, photon energy, band gap, and a constant, respectively. The  $n$  value depends on the characteristics of the transition in a semiconductor. For  $\text{BiOX}$ ,  $n$  is 4 for its indirect transition.

The UV-vis DRS of  $\text{Bi}_{12}\text{O}_{17}\text{Cl}_2$  nanobelts and  $\text{BiOCl}$  are shown in Fig. 6a. A red-shift of the absorption edge of  $\text{Bi}_{12}\text{O}_{17}\text{Cl}_2$  nanobelts could be observed, compared with that of  $\text{BiOCl}$ . In order to estimate the  $E_g$  value, the Tauc plots ( $(\alpha h\nu)^{1/2}$  vs.  $h\nu$ ) of  $\text{Bi}_{12}\text{O}_{17}\text{Cl}_2$  nanobelts and  $\text{BiOCl}$  (Fig. 6b) were calculated based on the UV-vis DRS. It is widely recognized that the semiconductor band gap is

governed by the linear Tauc region, which is just above the optical absorption edge [41]. Thus, the band gaps of  $\text{Bi}_{12}\text{O}_{17}\text{Cl}_2$  nanobelts and  $\text{BiOCl}$  were approximately 2.07 and 3.16 eV, respectively. The results indicate that the  $\text{Bi}_{12}\text{O}_{17}\text{Cl}_2$  nanobelts had a narrower band gap than  $\text{BiOCl}$ , and its absorption region occurred in visible light region.

The VB of  $\text{Bi}_{12}\text{O}_{17}\text{Cl}_2$  nanobelts and  $\text{BiOCl}$  were measured by XPS valence spectra. The VB position of the  $\text{Bi}_{12}\text{O}_{17}\text{Cl}_2$  nanobelts and  $\text{BiOCl}$  occurred at 1.51 and 1.63 eV, respectively (Fig. 6c). Therefore, the position of the CB can be calculated by the following equation:

$$E_g = E_{VB} - E_{CB} \quad (2)$$

where  $E_{VB}$  and  $E_{CB}$  are the valence band position, and conduction band position, respectively.

Taking their band gap and  $E_{VB}$  into consideration, the CB positions of  $\text{Bi}_{12}\text{O}_{17}\text{Cl}_2$  nanobelts and  $\text{BiOCl}$  were found to be  $-0.56$  eV and  $-1.53$  eV, respectively. The band relative position of  $\text{Bi}_{12}\text{O}_{17}\text{Cl}_2$  nanobelts and  $\text{BiOCl}$  are shown in Fig. 6d. It was observed that the corresponding colors of  $\text{Bi}_{12}\text{O}_{17}\text{Cl}_2$  and  $\text{BiOCl}$  products were yellow and white, respectively.

The standard redox potential of  $\text{O}_2/\cdot\text{O}_2^-$  is  $-0.33$  eV and is more positive than the CB position of  $\text{Bi}_{12}\text{O}_{17}\text{Cl}_2$  nanobelts ( $-0.56$  eV). Thus, the photogenerated electron ( $e^-$ ) can react with  $\text{O}_2$  to produce  $\cdot\text{O}_2^-$  and the following reaction occurs:



To verify the above reaction mechanism, nitroblue tetrazolium (NBT) was chosen to trap the  $\cdot\text{O}_2^-$ . The maximum absorbance in the UV-vis spectra of NBT declined prominently, indicating that  $e^-$  reacts with  $\text{O}_2$  to produce abundant  $\cdot\text{O}_2^-$  rapidly under visible light (Fig. 7a).

The standard redox potential of  $\cdot\text{OH}/\text{OH}^-$  is  $+2.38$  eV, which is more positive than the VB position of  $\text{Bi}_{12}\text{O}_{17}\text{Cl}_2$  nanobelts (1.51 eV). Thus, the photogenerated hole ( $h^+$ ) cannot react with

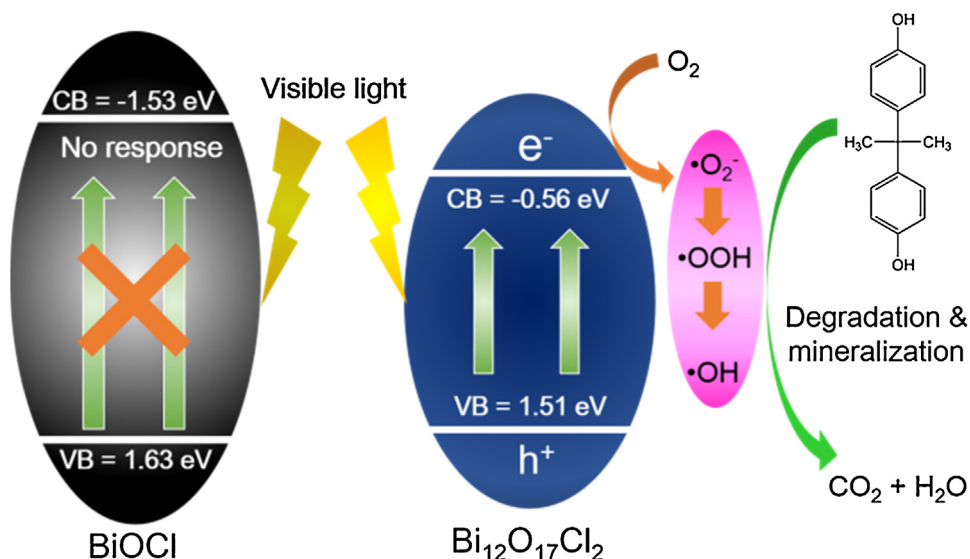


**Fig. 9.** Schematic of BPA degradation over  $\text{Bi}_{12}\text{O}_{17}\text{Cl}_2$ .

$\text{H}_2\text{O}$  to produce  $\cdot\text{OH}$  over  $\text{Bi}_{12}\text{O}_{17}\text{Cl}_2$  nanobelts. Therefore,  $\cdot\text{OH}$  is assumed to be produced via the following reactions:



To verify the assumption, the 5,5-dimethyl-1-pyrroline N-oxide (DMPO) spin-trapped ESR spectroscopy was used to track the active radicals formed. The  $\cdot\text{OOH}$  characterized by seven intensity peaks were detected in the presence of  $\text{Bi}_{12}\text{O}_{17}\text{Cl}_2$  (Fig. 7b), and the characteristic peaks of  $\cdot\text{OH}$  appeared in the presence of  $\text{Bi}_{12}\text{O}_{17}\text{Cl}_2$  (Fig. 7c), indicating that  $\text{Bi}_{12}\text{O}_{17}\text{Cl}_2$  could produce  $\cdot\text{OH}$  under visible light irradiation and confirm the assumptions above. However, compared to  $\text{Bi}_{12}\text{O}_{17}\text{Cl}_2$ , no obvious changes were observed in the UV-vis spectra of NBT in the  $\text{BiOCl}$  suspension (Fig. 7d), and no peaks appeared in the ESR spectra of  $\text{BiOCl}$  (Fig. 7e and f), indicating the inability of  $\text{BiOCl}$  for generating free radicals under visible light irradiation.

#### 3.4. BPA degradation pathway by $\text{Bi}_{12}\text{O}_{17}\text{Cl}_2$ nanobelts

To further explore the photocatalytic degradation mechanism of BPA, the intermediates formed in the photodegradation processes were analyzed by using LC-MS. The photocatalytic degradation of BPA occurred mainly through hydroxylation or  $\text{h}^+$ , and BPA was then degraded to carboxylic acid, formic acid, acetic acid, and eventually mineralized into  $\text{H}_2\text{O}$  and  $\text{CO}_2$ . In this work, BPA and other four intermediates were detected by LC-MS (Fig. S3). The concentration of BPA ( $m/z$  227) continuously decreased, indicating the degradation of BPA. The concentrations of two intermediates ( $m/z$  133 and 135) increased quickly in the initial 40 min, later became stable, and then decreased. This result suggests that the two intermediates were the primary products of BPA photodegradation. Furthermore, other two intermediates ( $m/z$  109 and 143) at a very low level were detected in the initial 40 min, but they existed at an almost a constant level after 60 min, indicating that the two intermediates ( $m/z$  109 and 143) were the secondary products generated from the two primary products. Thus, the BPA degradation process can be divided into three steps: cleaving, aromatic ring opening, and mineralizing, as shown in Fig. 8.

#### 3.5. Photocatalytic BPA degradation mechanisms over $\text{Bi}_{12}\text{O}_{17}\text{Cl}_2$ nanobelts

On the basis of the aforementioned results, the BPA degradation mechanism over the as-prepared  $\text{Bi}_{12}\text{O}_{17}\text{Cl}_2$  nanobelts under visible light irradiation could be proposed (Fig. 9). First, the  $\text{Bi}_{12}\text{O}_{17}\text{Cl}_2$  nanobelts absorb visible light, and separate the  $\text{h}^+-\text{e}^-$  pairs in irradiation. Then, chemisorbed  $\text{O}_2$  molecules are activated by  $\text{e}^-$  on the CB of  $\text{Bi}_{12}\text{O}_{17}\text{Cl}_2$  and plentiful  $\cdot\text{O}_2^-$  is produced through one-electron transfer, which is further converted into  $\cdot\text{OH}$  through a series of free radical reactions. Lastly, BPA in the solution is efficiently degraded by the generated active species. After cleaving and aromatic ring opening, BPA is finally mineralized into  $\text{CO}_2$  and  $\text{H}_2\text{O}$ .

## 4. Conclusions

In summary,  $\text{Bi}_{12}\text{O}_{17}\text{Cl}_2$  nanobelts were obtained by using a solvothermal route and exhibited a high photocatalytic activity under visible light. The BPA degradation rate by  $\text{Bi}_{12}\text{O}_{17}\text{Cl}_2$  nanobelts was 20 and 40 fold higher than those by  $\text{BiOCl}$  and  $\text{TiO}_2$  (P25), respectively. In the photocatalytic BPA degradation, large quantities of  $\cdot\text{O}_2^-$  were generated over  $\text{Bi}_{12}\text{O}_{17}\text{Cl}_2$  nanobelts because of their narrowed band gap. Then,  $\cdot\text{O}_2^-$  was changed into  $\cdot\text{OH}$  through a series of free radical reactions. Finally,  $\cdot\text{O}_2^-$  played a critical role to degrade BPA. The BPA degradation pathway was divided into three steps, cleaving, aromatic ring opening, and mineralizing. The excellent performance of  $\text{Bi}_{12}\text{O}_{17}\text{Cl}_2$  nanobelts indicates the effectiveness and feasibility of using this photocatalyst for organic pollutant degradation, and greatly expands the potential application of photocatalysts like bismuth oxychloride for water and wastewater treatment.

## Acknowledgements

This work is supported by the National Natural Science Foundation of China (51538011 and 21590812) and the Program for Changjiang Scholars and Innovative Research Team in University of the Ministry of Education of China and by the Open Project of State Key Laboratory of Urban Water Resource and Environment (QA201402).

## Appendix A. Supplementary data

Supplementary data associated with this article can be found, in the online version, at <http://dx.doi.org/10.1016/j.apcatb.2016.07.054>.

## References

- [1] H. Park, H.I. Kim, G.H. Moon, W. Choi, *Energy Environ. Sci.* 9 (2016) 411–433.
- [2] X. Chang, S. Wang, Q. Qi, M.A. Gondal, S.G. Rashid, D. Yang, M.A. Dastageer, K. Shen, Q. Xu, P. Wang, *Appl. Catal. B: Environ.* 176–177 (2015) 201–211.
- [3] H. Li, J. Shang, Z. Ai, L. Zhang, *J. Am. Chem. Soc.* 137 (2015) 6393–6399.
- [4] L. Ye, Y. Su, X. Jin, H. Xie, C. Zhang, *Environ. Sci. Nano* 1 (2014) 90–112.
- [5] W.K. Wang, J.J. Chen, M. Gao, Y.X. Huang, X. Zhang, H.Q. Yu, *Appl. Catal. B: Environ.* 195 (2016) 69–76.
- [6] D.N. Pei, L. Gong, A.Y. Zhang, X. Zhang, J.J. Chen, Y. Mu, H.Q. Yu, *Nat. Commun.* 6 (2015) 8696–8705.
- [7] C. Liu, A.Y. Zhang, D.N. Pei, H.Q. Yu, *Environ. Sci. Technol.* 50 (2016) 5234–5242.
- [8] A.O. Kondrakov, A.N. Ignatev, F.H. Frimmel, S. Bräse, H. Horn, A.I. Revelsky, *Appl. Catal. B: Environ.* 160–161 (2014) 106–114.
- [9] F. Tian, Y. Zhang, G. Li, Y. Liu, R. Chen, *New J. Chem.* 39 (2015) 1274–1280.
- [10] L. Ye, L. Zan, L. Tian, T. Peng, J. Zhang, *Chem. Commun.* 47 (2011) 6951–6953.
- [11] J. Li, L. Zhang, Y. Li, Y. Yu, *Nanoscale* 6 (2014) 167–171.
- [12] J. Jiang, K. Zhao, X. Xiao, L. Zhang, *J. Am. Chem. Soc.* 134 (2012) 4473–4476.
- [13] J. Li, K. Zhao, Y. Yu, L. Zhang, *Adv. Funct. Mater.* 25 (2015) 2189–2201.
- [14] K. Zhang, C. Liu, F. Huang, C. Zheng, W. Wang, *Appl. Catal. B: Environ.* 68 (2006) 125–129.
- [15] S. Ning, L. Ding, Z. Lin, Q. Lin, H. Zhang, H. Lin, J. Long, X. Wang, *Appl. Catal. B: Environ.* 185 (2016) 203–212.
- [16] L. Ye, X. Jin, C. Liu, C. Ding, H. Xie, K.H. Chu, P.K. Wong, *Appl. Catal. B: Environ.* 187 (2016) 281–290.
- [17] M. Guan, C. Xiao, J. Zhang, S. Fan, R. An, Q. Cheng, J. Xie, M. Zhou, B. Ye, Y. Xie, *J. Am. Chem. Soc.* 135 (2013) 10411–10417.
- [18] A.M. Ganose, M. Cuff, K.T. Butler, A. Walsh, D.O. Scanlon, *Chem. Mater.* 28 (2016) 1980–1984.
- [19] Y. Myung, F. Wu, S. Banerjee, A. Stoica, H. Zhong, S.S. Lee, J. Fortner, L. Yang, P. Banerjee, *Chem. Mater.* 27 (2015) 7710–7718.
- [20] X. Zhang, L.W. Wang, C.Y. Wang, W.K. Wang, Y.L. Chen, Y.X. Huang, W.W. Li, Y.J. Feng, H.Q. Yu, *Chem. Eur. J.* 21 (2015) 11872–11877.
- [21] X. Zhang, C.Y. Wang, L.W. Wang, G.X. Huang, W.K. Wang, H.Q. Yu, *Sci. Rep.* 6 (2016) 22800–22809.
- [22] J. Li, G. Zhan, Y. Yu, L. Zhang, *Nat. Commun.* 7 (2016) 11480–11488.
- [23] C.Y. Wang, X. Zhang, X.N. Song, W.K. Wang, H.Q. Yu, *ACS Appl. Mater. Interfaces* 8 (2016) 5320–5326.
- [24] X. Lin, T. Huang, F. Huang, W. Wang, J. Shi, *J. Phys. Chem. B* 110 (2006) 24629–24634.
- [25] X.Y. Chen, H.S. Huh, S.W. Lee, *J. Solid State Chem.* 180 (2007) 2510–2516.
- [26] L. Wang, J. Shang, W. Hao, S. Jiang, S. Huang, T. Wang, Z. Sun, Y. Du, S. Dou, T. Xie, *Sci. Rep.* 4 (2014) 7384–7391.
- [27] X. Xiao, C. Liu, R. Hu, X. Zuo, J. Nan, L. Li, L. Wang, *J. Mater. Chem.* 22 (2012) 22840–22843.
- [28] H. Deng, J. Wang, Q. Peng, X. Wang, Y. Li, *Chemistry* 11 (2005) 6519–6524.
- [29] X. Xiao, J. Jiang, L. Zhang, *Appl. Catal. B: Environ.* 142–143 (2013) 487–493.
- [30] L.C. Tien, Y.L. Lin, S.Y. Chen, *Mater. Lett.* 113 (2013) 30–33.
- [31] A. Alsbaee, B.J. Smith, L. Xiao, Y. Ling, D.E. Helbling, W.R. Dichtel, *Nature* 529 (2015) 190–194.
- [32] M. Pan, H. Zhang, G. Gao, L. Liu, W. Chen, *Environ. Sci. Technol.* 49 (2015) 6240–6248.
- [33] P. Valitalo, N. Perkola, T.B. Seiler, M. Sillanpää, J. Kuckelkorn, A. Mikola, H. Hollert, E. Schultz, *Water Res.* 88 (2016) 740–749.
- [34] N.A. Zhou, H. Kjeldal, H.L. Gough, J.L. Nielsen, *Environ. Sci. Technol.* 49 (2015) 12232–12241.
- [35] Z. Li, Y. Wu, G. Lu, *Appl. Catal. B: Environ.* 188 (2016) 56–64.
- [36] K. Ji, H. Dai, J. Deng, H. Zang, H. Arandiyani, S. Xie, H. Yang, *Appl. Catal. B: Environ.* 168–169 (2015) 274–282.
- [37] H. Li, L. Zhang, *Nanoscale* 6 (2014) 7805–7810.
- [38] H. Huang, X. Han, X. Li, S. Wang, P.K. Chu, Y. Zhang, *ACS Appl. Mater. Interfaces* 7 (2015) 482–492.
- [39] L. Yu, X. Zhang, G. Li, Y. Cao, Y. Shao, D. Li, *Appl. Catal. B: Environ.* 187 (2016) 301–309.
- [40] H. Tian, F. Teng, J. Xu, S. Lou, N. Li, Y. Zhao, M. Chen, *Sci. Rep.* 5 (2015) 7770–7778.
- [41] X.N. Song, C.Y. Wang, W.K. Wang, X. Zhang, N.N. Hou, H.Q. Yu, *Adv. Mater. Interfaces* 3 (2016) 1500417–1500423.